Electronic Supplementary Informatin (ESI)

Role of Two-Dimensional Monolayer MoS_2 Interlayer in the Temperature-Dependent Longitudinal Spin Seebeck Effect in Pt/YIG Bilayer Structures

Chanho Park[1, †], Jae Won Choi[1, †], No-Won Park[1] , Gil-Sung Kim[1] , Takashi Kikkawa[2], Eiji Saitoh[2,3,4], and Sang-Kwon Lee[1,*]

[1]Department of Physics, Center for Berry Curvature based New Phenomena, Chung-Ang University, Seoul 06974, Republic of Korea
[2]Department of Applied Physics, The University of Tokyo, Tokyo 113-8656, Japan
[3]Institute for AI and Beyond, The University of Tokyo, Tokyo 113-8656, Japan
[4]WPI Advanced Institute for Materials Research, Tohoku University, Sendai 980-8577, Japan

*Corresponding author. Email: sangkwonlee@cau.ac.kr
[†]These authors contributed equally to this work

1. X-ray Diffraction and Raman Patterns of the YIG/GGG Substrate

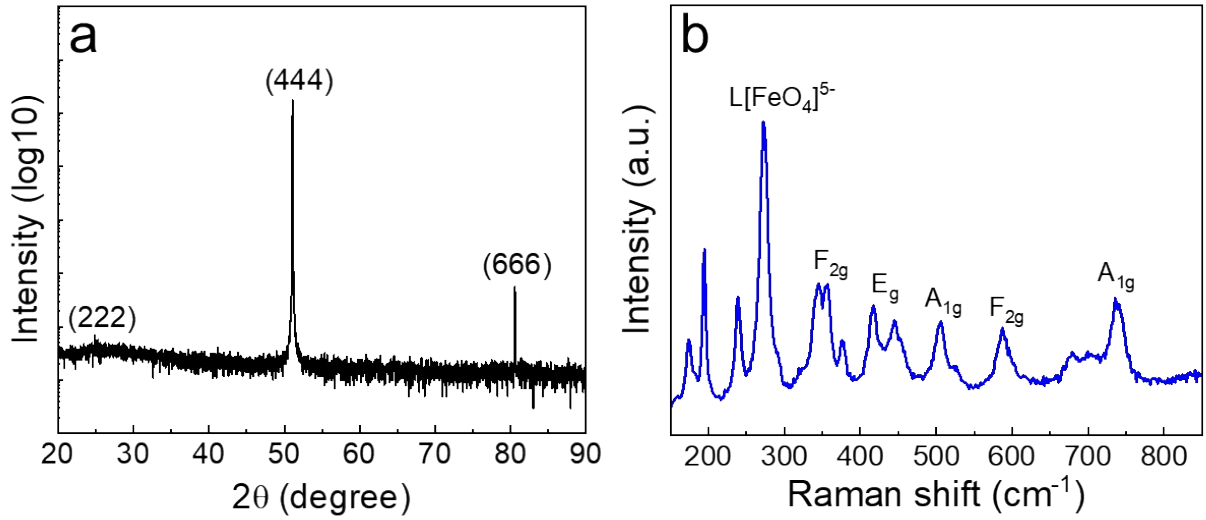

Fig. S1. Crystallographic and structural characterizations of the YIG/GGG structure. (a) X-ray diffraction pattern of the YIG/GGG substrate, showing only the (222), (444), and (666) Bragg peaks of YIG; no other phase is observed. (b) Raman spectrum of the YIG/GGG substrate. The Raman mode at ~ 272 cm^{-1} is labeled as $L[FeO_4]^{5-}$. The vibrations of the FeO_4 group form the internal Raman modes, which are labeled as F_{2g}, E_g, and A_{1g}. These Raman modes of our YIG/GGG substrate are in good agreement with those reported in previous studies on 15-nm-thick YIG/GGG thin films.[1] These results strongly suggest the achievement of a single-crystalline YIG growth with a [111] orientation on the [111]-oriented GGG (111) substrate.

2. Growth of triangular monolayer (ML) MoS_2

The monolayer (ML) MoS_2 flakes were synthesized by an atmospheric pressure chemical vapor deposition method with MoO_3 (99%, Aldrich) and sulfur (S) (99.5%, Aldrich) powders as sources. A hot wall furnace was used where the MoO_3 powder was placed in the center of a quartz tube. The S powder was placed in the upstream zone, whereas the SiO_2/Si substrate was placed face down above the crucible containing MoO_3. After pumping down to a base pressure of 60 mTorr and subsequently purging with high-purity N_2 gas to eliminate oxygen, the

temperature was gradually increased to 400 °C at a rate of 25 °C/min and maintained for 30 min, while the pressure was set to ~700 mTorr with a 100 sccm N_2 gas flow. After reducing the pressure to atmospheric conditions using 10 sccm N_2 gas flow, the temperature for the reaction was increased to 850 °C at a rate of 25 °C/min and maintained for 5 min for synthesis of monolayer MoS_2. Finally, the furnace was cooled down to room temperature naturally under same flow rate of carrier gas.

3. Wet transfer process for ML MoS_2 on the YIG/GGG substrate

As-grown MLs MoS_2 flakes have been successfully transferred onto the YIG/GGG substrate as following steps: (i) a poly-methyl-methacrylate (PMMA, MW ~ 350K, Sigma-Aldrich) solution spun onto the MoS_2 flakes and subsequently annealed at 110 °C for 30 s. (ii) The PMMA-supported $MoS_2/SiO_2/Si$ substrate was emerged into 5 wt% hydrogen fluoride (HF) solution for etching SiO_2 layer at room temperature. (iii) After 1 minutes, the PMMA-supported ML MoS_2 detached from SiO_2/Si substrate on the water surface using the interface floating method, followed by thoroughly rinse in deionized (DI) water bath several times to remove HF remnants from the MoS_2 surface. (iv) The detached PMMA/MoS_2 layer was transferred onto the YIG/GGG substrate from the water surface, and dried at the room temperature. (v) After heating up at 110ºC for expelling remaining H_2O and enhancing interfacial adhesion between MoS_2 and YIG/GGG, the MoS_2-transferred substrate was dipped into acetone bath for 2 h in order to remove PMMA. (vi) After gently drying using N_2 gas, the Pt layer was deposited onto the ML MoS_2/YIG/GGG samples by radio-frequency magnetron sputtering in ultrahigh vacuum at an ambient temperature.

4. Calculation of J_s using the BTE

One of the most straightforward methods to calculate spin current density in a normal metal (NM)/ferromagnetic (FM) system is the Boltzmann transport equation (BTE). Based on the drift-diffusion model of spins, one can semi-classically solve the BTE-attached magnon chemical potential stemming from the boundary conditions. Then, the charge current or voltage converted from the spin current by inverse spin Hall effect (ISHE) can be calculated.[2] As shown in the paper, we directly followed the calculation steps of Rezende *et al*.[3] From the BTE model for the thermally driven longitudinal spin Seebeck effect (LSSE), the spin current J_S can be written in terms of the magnon relaxation time τ_k, magnetization, and other integrals used in describing the magnon distribution.[3] In the last step, instead of substituting a constant relaxation time for the magnons (τ_k) and another factor known as magnon scattering rate, we inserted the temperature-dependent magnon relaxation time $\tau(T)$ derived by Basso *et al*.[4]

Description of the one-dimensional spin current density: Magnons are generated due to the nonequilibrium magnetization in the YIG/GGG substrate.[5] We first need to solve the Landau–Lifshitz–Gilbert (LLG) equation for determining the magnetization dynamics.

$$\frac{dM}{dt} = -\gamma(M \times H_{eff}) + \frac{\alpha}{M_s}\left(\frac{dM}{dt} \times M\right), \quad (1)$$

where M is the magnetization vector for the YIG/GGG substrate, γ is the gyromagnetic ratio, α is the Gilbert damping constant, and M_s refers to the saturation magnetization. In our case, the interface of the sample is two-dimensional. Nevertheless, we can expand the one-dimensional spin wave propagation to two dimensions by integrating J_S later.[6] For instance, we can assume that the propagation of the spin wave is along z axis (in our experiment, the

injected spin wave propagates along the z direction, see Figure 1 in the main text), and there is no damping for the ideal case; thus, from the LLG equation, we can extract the form: $J_S = \gamma\frac{D}{M}(M \times \nabla M)$ using the continuity equation $\frac{d\rho}{dt} + \nabla \cdot J = 0$ for the magnetization current[6] or from the fluctuation-dissipation theorem for a random magnetic field due to temperature gradient and electron spin density in NMs (here, Pt).[7] Here, we employed the former case. Considering an effective magnetic field $\mathbf{H}_{\text{eff}}$ as

$$\mathbf{H}_{\text{eff}} = K\frac{M_z}{M}\hat{z} + D\nabla^2\frac{M}{M}, \quad (2)$$

where K is the anisotropy constant, and D is the exchange constant, which is related to stiffness, we then extracted only the z component (spin-wave propagating direction) of $\frac{\partial M}{\partial t} = -M \times K M_z\hat{z} - \frac{\partial J_s}{\partial z}$, which is obtained by substituting Eq. (2) into Eq. (1).[6] In the z direction, $\frac{\partial M}{\partial t} = -M \times K M_z\hat{z} - \frac{\partial J_s}{\partial z}$ becomes $\frac{\partial M}{\partial t}|_z = -\frac{\partial J_s}{\partial z}|_z$, which is the form $\frac{d\rho}{dt} + \nabla \cdot J = 0$, and thus, we can to define $J_S = \gamma\frac{D}{M}(M \times \nabla M)$ as the magnetization current.[8]

BTE analysis (diffusion): Since the spin current is the transport phenomena mediated by magnons, based on the conservation of angular momentum,[3] BTE must include the distribution of the magnons with appropriate boundary conditions. [2]

$$0 = -v_k \cdot \nabla_r f - \frac{1\partial f}{\hbar\partial k} \cdot \hbar\frac{dk}{dt} + \frac{f_0 - f}{\tau(k)}, \quad (3)$$

where f denotes the magnon distribution, $\left(\frac{df}{dt}\right)_{scatt.}$ is the rate of magnon decay due to

scattering,[3] f_0 is the distribution of equilibrium magnon states, and $\tau(k)$ is the relaxation time.[8]

To use $J_S = \gamma\frac{D}{M}(M \times \nabla M)$, quantum operators for circularly polarized magnons must be established, i.e., $m^+ = (\frac{2\gamma\hbar M}{V})^{1/2}\sum_k e^{ikr}c_k$, where c_k is the magnon annihilation operator,[8] V is the volume of the system, and $(\frac{2\gamma\hbar M}{V})^{1/2}$ denotes the energy unit over the volume due to magnetization. The root mean square method was adopted to express $m^+ m^-$. By substituting these operators, $J_S = \gamma\frac{D}{M}(M \times \nabla M)$ can be expressed as

$$J_S = \frac{\hbar}{V}\sum_k n_k v_k \quad , \tag{4}$$

where $n_k = c_k c^+_k$ is the number operator. After replacing the sum over the Brillouin zone, Eq. (4) can be written as, with an equilibrium number of magnons, n_0,

$$J_{S,\nabla n} = \frac{-\hbar}{(2\pi)^3}\int d^3k\, \tau(k) v_k [v_k \cdot \nabla(n_k - n_0)] \quad , \tag{5}$$

BTE analysis (temperature gradient): Rezende *et al*. noted that the spin current pumped by the thermal gradient, which causes a difference in the Bose–Einstein distribution leading to a nonequilibrium excess of magnons, must be taken into account.[8] Considering the units in Eq. (5), the injected spin current due to the temperature gradient can be written as

$$J_{S,\nabla T} = \frac{-\hbar}{(2\pi)^3}\int d^3k\, \tau(k)\frac{\partial n_k}{\partial T} v_k [v_k \cdot \nabla T] \quad . \tag{6}$$

Therefore, the overall injected spin current is $J_{S,\nabla n} + J_{S,\nabla T}$, which is obtained after performing

different algebraic operations, such as changing the variables and rearrangement of some factors, and by determining the unknown coefficients using the boundary conditions in the diffusion theory. We finally obtain the injected spin current at the interface (z = 0)

$$J_s = \frac{g_{eff}^{\uparrow\downarrow}\sqrt{\tau_k}\sqrt{\tau_{mp}}\pi\,\gamma\,k_m^2 k_B w_{ZB}}{4\pi M} \frac{\frac{1}{(2\pi)^3}\int d^3k\,\frac{x^2}{(e^x - 1)}\,\frac{\hbar}{(2\pi)^3}\int d^3k\,v_k^2\,\frac{}{(e^}}{\sqrt{\frac{1}{(2\pi)^3}\int d^3k\,\frac{x}{(e^x - 1)}}\,\sqrt{\frac{1}{(2\pi)^3}\int d^3}} \quad (7)$$

where $\hbar$ is Planck's constant, $g_{eff}^{\uparrow\downarrow}$, τ_k, τ_{mp}, γ, k_m, k_B, and w_{ZB} are effective spin mixing conductance, the relaxation time for the magnons, magnon–phonon relaxation time, gyromagnetic ratio, value of the maximum wavenumber in the spherical Brillouin zone , Boltzmann's constant, and zone boundary frequency, respectively.[3, 8] Further, k_m and w_{ZB} are obtained from the magnon dispersion relation (w_k) in YIG. Note that we used a correction factor for $g_{\uparrow\downarrow}$ by considering various ranges of the spin-mixing conductance reported in other literatures.

Integrals in J_s: Here, we changed the variable dependence of τ_k from k to T to substitute the value reported by Basso *et al*. When substituting $\tau(T)$, Matthiessen's rule for $\tau(T)$ at low (high) temperature is applied.[4] From Eq. (7), we must compute four integrals using $x = \frac{\hbar\, w_k}{K_B T}$. The magnon dispersion relation (for YIG) is given by: $w_k = \gamma H + w_{ZB}\left(1 - \cos\left(\frac{\pi\, k}{2k_m}\right)\right)$,[9] where w_{ZB} is the zone boundary frequency,[8] and v_k can be obtained by differentiating the dispersion

relation. By substituting w_k in $x = \frac{\hbar w_k}{K_B T}$, Eq. (7) can be calculated by numerical integration and using the values listed in Table S1 and S2.

After substituting the results into Eq. (7) , V_{ISHE} is obtained using the following equation: [10]

$$V_{ISHE} = R_{ML} w \lambda_{NM} \left(\frac{2e}{\hbar}\right) \theta_{SH} \tanh\left(\frac{t_{NM}}{2\lambda_{NM}}\right) J_s, \quad (8)$$

where R_{ML}, w, λ_{NM}, θ_{SH}, and t_{NM} are the resistance, sample width, Pt diffusion length, spin hall angle, and Pt thickness, respectively. By inserting all the related values into Eq. (7), Eq. (8) (i.e., R_{ML} = 125 Ω for Pt/YIG in our measurement; $g_{eff}^{\uparrow\downarrow} = C\, g^{\uparrow\downarrow}$ with C as the correction factor as $g^{\uparrow\downarrow}$ varies from that reported in the literature[8]), we computed the total theoretical V_{ISHE} of the Pt/YIG structure. In this paper, three methods of evaluating V_{ISHE} are discussed. Rezende *et al*. used the magnon scattering rate with 3–4 magnon scattering processes for treating τ_k.[3, 8] To discuss the magnon scattering, different magnon mean collision times depending on the temperature must be considered. [4] For magnons at a low temperature, scattering with phonons and defects dominates over pure magnon–magnon scattering because of the small number of magnon filled states and phonon lifetime in the FM substrate. [3, 11] By contrast, at high temperatures, magnon–magnon scattering is also taken into account, which results in different orders of temperature-dependence of the magnon relaxation time compared to those at low temperatures.[4] Thus, we substituted the temperature dependent magnon relaxation time $\tau(T)$, derived from thermo-magneto dynamic calculations, and the experimental spin Seebeck coefficients, which correspond well with experimental results of Basso *et al*.[4, 12] We compared

the two calculation results in advance. First, the temperature-dependent V_{LSSE} was compared by inserting $\tau(T)$, where original relaxation time τ is replaced with $\tau(T)$ in the standard BTE model (A).[4] Next, we calculated the temperature-dependent V_{LSSE} by inserting both $\tau(T)$ and the scattering rate n_q reported by Rezende *et al*. (B).[3] Both the calculations included some integrals, which were numerically computed for 10 K intervals over the temperature range of 0–300 K. The resulting values from (A) and (B) are consistent with each other at T = 300 K, because the original magnon relaxation time τ_k is defined differently depending on previous studies.[3, 4, 8, 9] At a high temperature range of 200–300 K, both (A) and (B) show almost the same decreasing tendencies (Fig. S2), indicating that sufficient magnon–magnon interactions occur; both n_q and $\tau(T)$ are based on magnon–magnon interactions and relaxation mechanisms.[3, 4] In contrast, at low temperature range (0–100 K), discrepancies occur because of various reasons: the magnon–magnon scattering at low temperatures is not frequent (in contrast to those at high temperatures); rather, phonon mediated effects may dominant (discussed in the next subsection).[11, 13] Further, the dispersion relation slightly changes with temperatures,[3] because we have fixed the magnon dispersion relation at all the temperatures and also included scattering rates in the integral at low temperatures in (B) case. However, it cannot be declared that either of these results is right or wrong, for that one has substituted the value extracted from magneto-thermodynamics and spin Seebeck experiment, while another one has inserted the values from conventional scattering theory. We finally compared the computational result by inserting n_q only, similar to the calculations of Rezende *et al*. (C). However, at T = 200–300 K, (C) shows much less voltage decreasing tendencies than (A) and (B) and rather shows saturation values at high temperatures (Fig. S2). Rezende *et al.* included an additional temperature dependence of the magnon relaxation rate, which vary with T^2, and the temperature dependence of the magnetization of the YIG/GGG substrate to obtain results

that are consistent with the experiment results. [8] Among these computational results, based on the fact that we observed nearly same tendencies for temperature dependent LSSE voltage at high temperatures (200–300 K), and in order to use (C) we must take steps adding arbitrary temperature dependence of magnon relaxation rates and magnetization, we rather decided to compare the experimental value with the calculation result (A), where temperature-dependent magnon collision time is incorporated in $\tau(T)$.

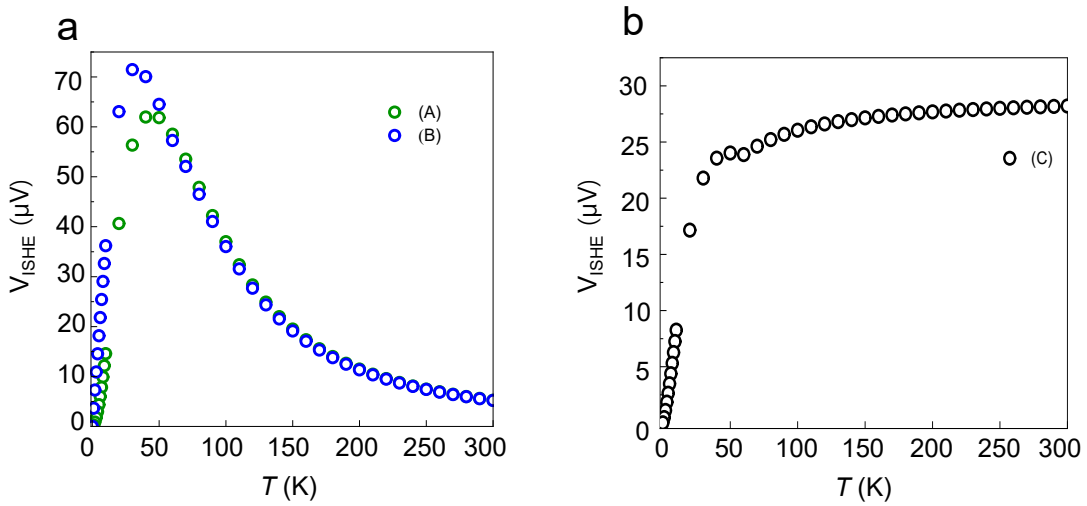

Fig. S2. Calculations of V_{ISHE} based on the BTE model. (a) is (A) V_{ISHE} with the substitution of $\tau(T)$ derived by Basso *et al.* into BTE model, (B) V_{ISHE} with $\tau(T)$ (from Basso *et al.*) and n_q (from Rezende *et al.*) both inserted into BTE model. (b) is (C) V_{ISHE} with n_q inserted only, where τ_k^0 (τ_k with k around the zone center) remains constant. Among these results, (C) does not exhibit an actual temperature-dependent V_{ISHE} behavior owing to the absence of T dependence of τ_k (it was included later in Rezende's work).

Meanwhile, with the experimental results in Pt/YIG bilayer we extracted mean magnon collision time, or magnon scattering time at high temperature (T = 180–200 K) from the expressions from Eq. (7)–(8) to see if the BTE method combined with $\tau(T)$ is in good agreement compared with other studies (Fig. S3). From Basso's work, at high temperature the

magnon scattering time have shown T^{-4} dependence.[4] In our computations from the experiments, magnon scattering time have shown -4.07 $\pm$ 009 order of T , which is similar to the result of Basso *et al.*. The exact value of the magnon scattering time may differ from the studies from Basso, since ordinary constant value of τ_k varies from studies and other works[4, 8, 9].

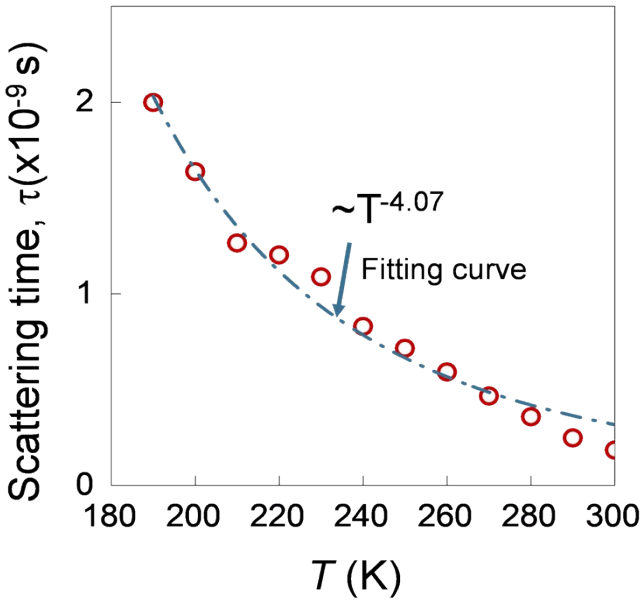

Fig. S3. (a) Magnon collision time or magnon scattering time for the Pt/YIG bilayer structure obtained from the LSSE measurement. Evidently, the extracted magnon scattering time follows a nearly T^{-4} dependence, similar to the results of Basso *et al.*

5. Temperature dependence of V_{ISHE} by thermally driven magnons

Next, we analyzed properties of thermally driven magnons at low temperatures based on the calculation from BTE model. One of the expressions used for estimating J_s is mentioned below:

$$J_s \sim \int dx \frac{\pi^2 \sqrt[3]{32} k_B T}{(\hbar w_{ZB} \pi^2)^{5/2}} (\sqrt{32(k_B T x - \hbar\gamma H)})^3 \frac{e^x x}{(e^x - 1)^2}, \quad (10)$$

where it is integrated with respect to $x = \frac{\hbar w_k}{K_B T}$. Other integrals in the form of Eq. (10) are also present in J_s (See Eq. (7)). As the integrand has *T* terms in the numerator, it seems that the overall J_s, which is proportional to V_{ISHE}, tends to shrink as *T* decreases. However, for the variable *x*, its integrating interval ranges from $x = 0$ to $x = \frac{\hbar w_k}{K_B T}$, where T in the denominator indicates that the integrating range is inversely proportional to T. When considering thermally driven magnons only, at high temperatures the integrating range for thermal magnons, $x = \frac{\hbar w_k}{K_B T}$, dominates as T holds some finite value. As T slowly reaches toward low temperature (~50 K), the size of the integration range dominates over the T terms in the integrand. However, at low temperature if T reaches toward 0K (< 50 K), the T terms in the integrand again hold some leverage on the whole integral as *T* runs toward 0 K; hence, the overall J_s starts to drop and reaches 0 μV at *T* = 0 K in theoretical calculations. Fig. 4c–d in the main text compares the calculated V_{ISHE} values at each temperature (red symbols for Pt/YIG and blue symbols for Pt/ML MoS_2/YIG) with the experimental V_{ISHE} values (green symbols). Both Pt/YIG, Pt/ML MoS_2/YIG follows increasing V_{ISHE} tendencies from *T* = 300 K to 190 K, and error bounds between the theoretical evaluation and the experimental values are marked in the figure. At the low temperature range, *T* = 0–100 K, according to the calculation we observed critical temperature at which the V_{ISHE} reaches maximum value. For Pt/YIG bilayer case (Fig. 4c), the maximum temperature dependent V_{ISHE} was approximately 62 μV, whereas that of Pt/ML MoS_2/YIG trilayer case was 3.55 μV. Note that we have conducted experiments at high temperatures only, *T* = 190–300 K to observe the magnon behavior close to room temperature. Nevertheless, the calculations for the low temperature range indicate that the experimental

V_{ISHE} would also maximize at around T = 40–50 K and then decrease toward 0 μV as T reaches 0 K.

The temperature-dependent behavior of the magnons based on the physics is discussed. At high temperature, under the state of thermally excited magnons, as in our case, they have some limited filled states at some T at high temperature.[8, 9] At low temperature region, magnon – magnon scattering does not occur frequently than it was at high temperatures, rather, phonon mediated effect may have been considered to be significant.[11, 13] Basically, phonons are less excited at low temperatures while magnons follow typical quadratic dispersion relations at low temperatures, thus having less chance for magnon-phonon interaction.[8, 11, 14] Calculated curves from the figures at the temperature range from T = 0 to 40 K can be interpreted as increasing contribution of the excited phonon to the system as T increases. At the vicinity of the maximum V_{ISHE}, a Umklapp scattering region exists, which limits the blindly increasing phonon excitations and contributes to the T^{-1} dependence above the critical temperature.[11, 14, 15] Above the critical temperature, the magnon–phonon interactions possibly cause some deviation from the T^{-1} dependence, where now significant amount of magnons are driven so that the interaction between magnon and phonon becomes inevitable. However, this suggested mechanism still needs to be verified clearly through future studies.[4, 11, 16]

Table S1. Parameters for calculating J_s of the Pt/YIG bilayer. The magnon–phonon relaxation time, gyromagnetic ratio, magnon maximum wavenumber, and zone boundary frequency are taken from the literature in CGS units.[3]

Parameter	Value	Parameter	Value
τ_{mp}(s^{-1})	1.0 × 10^{12}	k_m(cm^{-1})	1.7 × 10^{7}
γ (GHz/kOe)	$2\pi \times$ 28	w_{ZB} (THz)	14π

Table S2. Parameters for calculating V_{ISHE} of the samples. The spin diffusion length λ_{Pt} and spin mixing conductance $g_{\uparrow\downarrow}$ (per unit area) of the Pt/YIG bilayer and Pt/ML MoS_2/YIG trilayer, respectively, are taken from previous syudies.[3, 17] Specifically, λ_{Pt} for the Pt/ML MoS2/YIG trilayer is obtained from the ratio between $\lambda_{Pt(Pt/YIG)}$ and $\lambda_{Pt(Pt/MoS2/YIG)}$, reported in other studies.[18, 19] Conversely, when calculating J_s from V_{ISHE}, $g_{\uparrow\downarrow}$ is converted to the unit of $\Omega^{-1}m^{-1}$ to fit in the units for Equation (3) from the main paper.

Sample	σ_{Pt} (S/m)	t_{Pt} (nm)	λ_{Pt} (nm)	$g_{\uparrow\downarrow}$ (cm^{-2})
Pt/YIG	2.00×10^6	5	3.7[3]	1.0×10^{14}
Pt/ML MoS_2/YIG	2.44×10^6	5.7	1.85	5.0×10^{13}

6. References

1. Li, M.; Jin, L.; Zhong, Z.; Tang, X.; Yang, Q.; Zhang, L.; Zhang, H., Impact of interfacial chemical state on spin pumping and inverse spin Hall effect in YIG/Pt hybrids. *Phys. Rev. B* **2020,** *102* (17), 174435.
2. Cornelissen, L. J.; Peters, K. J. H.; Bauer, G. E. W.; Duine, R. A.; van Wees, B. J., Magnon spin transport driven by the magnon chemical potential in a magnetic insulator. *Phys. Rev. B* **2016,** *94* (1), 014412.
3. Rezende, S. M., *Fundamentals of magnonics*. Springer: 2020; Vol. 969.
4. Basso, V.; Sola, A.; Ansalone, P.; Kuepferling, M., Temperature dependence of the mean magnon collision time in a spin Seebeck device. *J. Mag. Mag. Mater.* **2021,** *538*, 168289.
5. Ohnuma, Y.; Matsuo, M.; Maekawa, S., Theory of the spin Peltier effect. *Phys. Rev. B* **2017,** *96* (13), 134412.
6. Yan, P.; Wang, X. S.; Wang, X. R., All-magnonic spin-transfer torque and domain wall propagation. *Phys. Rev. Lett.* **2011,** *107* (17), 177207.
7. Ohe, J.-i.; Adachi, H.; Takahashi, S.; Maekawa, S., Numerical study on the spin Seebeck effect. *Phys. Rev. B* **2011,** *83* (11), 115118.
8. Rezende, S. M.; Rodríguez-Suárez, R. L.; Cunha, R. O.; Rodrigues, A. R.; Machado, F. L. A.; Fonseca Guerra, G. A.; Lopez Ortiz, J. C.; Azevedo, A., Magnon spin-current theory for the longitudinal spin-Seebeck effect. *Phys. Rev. B* **2014,** *89* (1).
9. Rezende, S. M.; Rodríguez-Suárez, R. L.; Lopez Ortiz, J. C.; Azevedo, A., Thermal properties of magnons and the spin Seebeck effect in yttrium iron garnet/normal metal hybrid structures. *Physical Review B* **2014,** *89* (13), 134406.
10. Shikoh, E.; Ando, K.; Kubo, K.; Saitoh, E.; Shinjo, T.; Shiraishi, M., Spin-pump-induced spin transport in p-type Si at room temperature. *Phys. Rev. Let.t* **2013,** *110* (12), 127201.
11. Iguchi, R.; Uchida, K.-i.; Daimon, S.; Saitoh, E., Concomitant enhancement of the longitudinal spin Seebeck effect and the thermal conductivity in a Pt/YIG/Pt system at low temperatures. *Phys. Rev. B* **2017,** *95* (17), 174401.
12. Basso, V.; Ferraro, E.; Magni, A.; Sola, A.; Kuepferling, M.; Pasquale, M., Nonequilibrium

thermodynamics of the spin Seebeck and spin Peltier effects. *Phys. Rev. B* **2016,** *93* (18), 184421.
13. Uchida, K.; Ota, T.; Adachi, H.; Xiao, J.; Nonaka, T.; Kajiwara, Y.; Bauer, G. E. W.; Maekawa, S.; Saitoh, E., Thermal spin pumping and magnon-phonon-mediated spin-Seebeck effect. *J. Appl. Phys.* **2012,** *111* (10), 103903.
14. Boona, S. R.; Heremans, J. P., Magnon thermal mean free path in yttrium iron garnet. *Phys. Rev. B* **2014,** *90* (6), 064421.
15. Ashcroft, N. W.; Mermin, N. D., Solid State Physic Holt. *Rinehart and Winston, New York, USA* **1976**.
16. Adachi, H.; Uchida, K.-i.; Saitoh, E.; Ohe, J.-i.; Takahashi, S.; Maekawa, S., Gigantic enhancement of spin Seebeck effect by phonon drag. *Appl. Phys. Lett.* **2010,** *97* (25), 252506.
17. Mendes, J. B. S.; Aparecido-Ferreira, A.; Holanda, J.; Azevedo, A.; Rezende, S. M., Efficient spin to charge current conversion in the 2D semiconductor MoS_2 by spin pumping from yttrium iron garnet. *Appl. Phys. Lett.* **2018,** *112* (24), 242407.
18. Kalappattil, V.; Geng, R.; Das, R.; Pham, M.; Luong, H.; Nguyen, T.; Popescu, A.; Woods, L. M.; Kläui, M.; Srikanth, H., Giant spin Seebeck effect through an interface organic semiconductor. *Mater. Horiz.* **2020,** *7* (5), 1413-1420.
19. Lin, W.; Chen, K.; Zhang, S.; Chien, C. L., Enhancement of Thermally Injected Spin Current through an Antiferromagnetic Insulator. *Phys. Rev. Lett.* **2016,** *116* (18), 186601.